Available online at www.sciencedirect.com
SCIENCE DIRECT®
ELSEVIER
Nuclear Instruments and Methods in Physics Research B 238 (2005) 205–213
NIM B
Beam Interactions with Materials & Atoms
www.elsevier.com/locate/nimb

A new small angle X-ray scattering station at NSRRC

Y.H. Lai, Y.S. Sun, U. Jeng *, Y.-S. Huang, Y.F. Song, R. Dronyak, K.L. Tsang, K.S. Liang

National Synchrotron Radiation Research Center, 101 Hsin-Ann Road, Hsinchu Science Park, Hsinchu 30076, Taiwan

Available online 8 August 2005

Abstract

Using the X-ray source generated by a newly installed superconducting wavelength shifter at the Taiwan Light Source storage ring of the National Synchrotron Radiation Research Center (NSRRC), we have constructed an X-ray beamline equipped with a small angle X-ray scattering (SAXS) station for nanostructure research. This beamline can deliver a photon flux of $\sim 3 \times 10^{11}$ photons/s in the energy range of 5–22 keV, with a beam divergence of $\sim$0.3 mrad in vertical direction. With the new SAXS end station we have studied PtRu nanoparticles embedded in fine carbon grains using anomalous SAXS. We illustrate other features of the SAXS instrument with a few more measurements on phase transitions of diblock-polymers, structural evolution of aluminium alloys under an artificial aging at high temperature, and folding and unfolding of lysozyme in aqueous solutions.
© 2005 Published by Elsevier B.V.

PACS: 61.10.Eq; 61.46.+w; 42.70.Jk; 87.15.−v; 61.82.Bg

Keywords: SAXS; Nanoparticles; Polymers; Biomolecules; Al alloy

1. Introduction

Small angle X-ray scattering (SAXS), carrying structural information of a resolution down to sub-nanometer, is widely used in many fields where nanostructures take decisive roles in determining phases, functions and/or performances of the subjects studied. Countless SAXS users and their fruitful results are boomed out by the rapid progresses in X-ray sources and instrumentation. Nowadays, one dedicated SAXS station nearly becomes an imperative in a synchrotron radiation facility. With photons of tremendously high flux in a wide energy range, many advanced synchrotron radiation based SAXS stations are further designed for specific research fields. For instances, the SAXS station of SPring-8 RIKEN beamline BL45XU aims at solution structures of proteins

* Corresponding author. Tel.: +886 35780281; fax: +886 35783813.
E-mail address: usjeng@nsrrc.org.tw (U. Jeng).

0168-583X/$ - see front matter © 2005 Published by Elsevier B.V.
doi:10.1016/j.nimb.2005.06.050

[1], and the SAXS/WAXS station X27C at NSLS, BNL, for polymer researches [2]. There are also versatile SAXS/WAXS stations like those at ID02 beamline of ESRF [3] and the SAXS beamline of Elettra [4], just to name a few. Most of the modern SAXS stations mentioned are characterized by their capability in doing time-resolved SAXS measurements, with a resolution even down to the order of millisecond.

Very recently, the National Synchrotron Radiation Research Center (NSRRC) has installed a superconducting wavelength shifter (SWLS) insertion device into the 1.5 GeV storage ring. This SWLS, composing of three magnet poles for a maximum magnetic field strength of 6 T, can shift the photon characteristic energy of the synchrotron radiation from 2 keV to 9 keV, thus, provides a hard X-ray source of 20 mrad horizontal radiation [5]. From the central 3 mrad of the horizontal radiation fan, BL01b beamline is constructed for general scattering purpose. We take the opportunity to setup a SAXS instrument temporarily for testing the beam performance and also conducting several SAXS measurements, before an advanced X-ray nanoimaging scope installed to the BL01b end station in the very near future.

2. Instrument components

2.1. Optics

The X-ray beam, of a vertical divergence of ~0.3 mrad, is extracted from the SWLS source and focused by a water-cooled toroidal mirror (FM) to the detector position (see Fig. 1 for the layout), with a focused beam size of 1.0 mm by 1.5 mm in the vertical and horizontal directions, respectively. The 3.0 mrad incident angle of the beam on the Rh-coated FM provides a reflectivity of 90% for 22 keV photons. Ge (1 1 1) double crystal monochromator DCM is used for monochromating the beam for an energy between 5 keV and 22 keV and an energy resolution $\Delta E/E$ of $\sim 10^{-3}$. The photon flux measured in this energy range is $\sim 3 \times 10^{11}$ photons/s at the sample position. Before the beam entering into the end station, there are four sets of slits arranged along the 26 m long beamline for controlling the beam divergence.

2.2. Front end of the SAXS instrument

The front end of the SAXS instrument includes beam collimation system, laser alignment system, beam attenuator and monitors (see Fig. 2), which are detailed in the following.

2.2.1. Beam collimation system

In the end station, there are two sets of pinholes separated by 970 mm for beam collimation. However, to save the limited space of the end station, we utilize the fourth set of slits in the beamline and the first set of pinholes (P1) in the end station for major collimation, which combination can control easily the beam divergence within 0.1 mrad due to the large separation (~4.8 m) between these two components. The second pinhole system (P2)

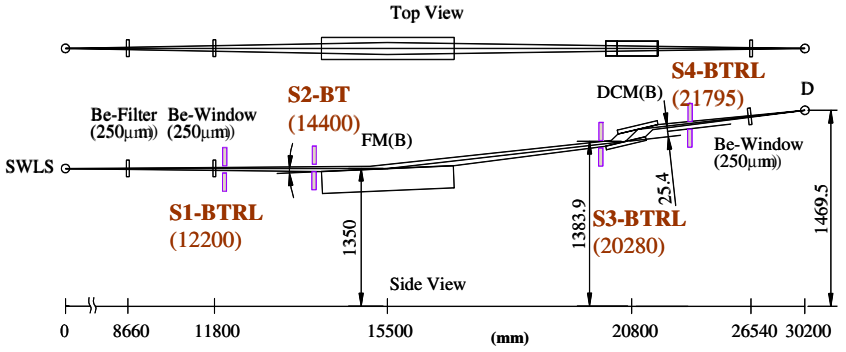

Fig. 1. Layout for the optical components of the BL01b beamline, including Be window, toroidal focusing mirror (FM), DCM and four sets of slits S1–S4. Symbols B, T, R and L represent slit blades in the bottom, top, right and left directions, respectively. The scale (mm) at the bottom indicates the relative positions of the components.

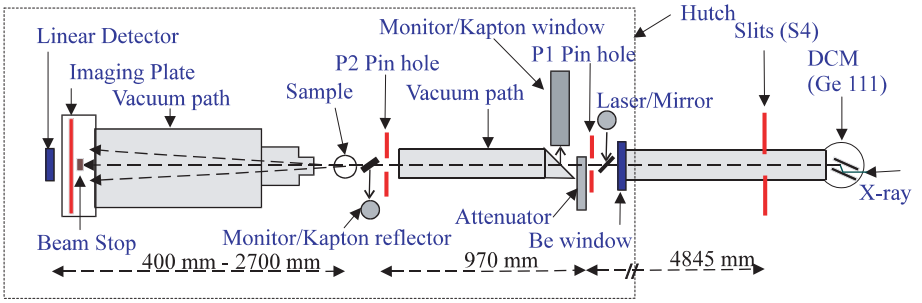

Fig. 2. Schematic view of the SAXS instrument at NSRRC.

in the end station is, then, used mainly for guarding parasite scattering. Each pinhole system provides options of 0.5, 0.75 or 1.0 mm dia. pinhole made from 1 mm thick tantalum (Ta) disk. All Ta pinholes are cut with a 5° angle to reduce possible parasite scatterings from the pinhole edge scattering.

2.2.2. Laser alignment system

With a semiconductor laser and a reflector on a stage of four degrees of freedom in rotation and translation, we can easily pass the laser light through the two sets of pinholes. The aligned visible laser beam provides quick and accurate alignments of samples, beam stopper and detector slits.

2.2.3. Beam attenuator

The attenuator sitting right behind P1 (see Fig. 2) contains 20 channels of attenuation distributed equally on an Al disk of a diameter of 14 cm. Combination of Al, Cu and Bi foils are used in the channels for attenuating the direct beam (5–22 keV) with fine steps, when sample scattering intensity is too strong and may damage the detectors.

2.2.4. Intensity monitors

Behind the pinhole system P1, we have a 45° titled thin Kapton window for sealing the vacuum pipe between P1 and P2, and meanwhile reflecting partially the direct beam into a NaI scintillation counter sitting right above the Kapton window. This NaI counter is used for the alignment of P1 pinhole as well as a beam intensity monitor. A Kapton reflector and a second NaI detector placed behind P2 are used for the P2 pinhole alignment.

2.2.5. Sample stage, holder and environmental control

The sample stage is equipped with four degrees of motions including rotation, translation and titling, for positioning samples to traditional transmission type of SAXS or grazing incidence SAXS (GISAXS) measurements. A sample cell, capable of sealing bulk or solution samples of various sizes and thicknesses, is designed for temperature-dependent SAXS measurement between −30 °C and 300 °C. Sample temperature can be ramped up or down between 20 °C and 150 °C within a few minutes, which is appropriate for slow dynamics in certain polymer systems. The whole sample cell (including solution samples) can also be sealed in vacuum or under various pressures, gases or humidity for SAXS measurements.

2.3. Post-sample section

The post-sample section of the SAXS instrument includes the vacuum pipe, beam stopper and detector system. The length of the vacuum chamber between sample and detector is adjustable between 400 mm and 2700 mm, for covering different Q ranges and resolutions required by specific measurements. Here, the wave vector transfer of scattered photons $Q = 4\pi \sin(\theta/2)/\lambda$ is defined by the scattering angle θ and wavelength λ. To reduce parasite scattering, we use 8 μm thick Kapton window of 20 mm dia. for sealing the entrance of the post-sample vacuum pipe, and 12 μm think Kapton window for the exit of the pipe. The exit is a long cross-shape opening with 200 mm in length and 10 mm in width to accommodate the linear detectors used.

Table 1
The characteristics of the SAXS instrument at NSRRC

Energy range	5–22 keV
Energy resolution	$\Delta E/E \sim 10^{-3}$
Focusing mirror	Toroidal mirror/1:1 focusing ratio
Monochromator	DCM, Ge (1 1 1)
Beam size	0.05–1 mm
Slit size	0.05–4 mm
Pinhole size	0.5, 0.7, 1, 1.25 mm
Flux (1.5×1.0 mm^2)	$\sim 3 \times 10^{11}$ photons/s (5–22 keV)
Sample-detector	400–2700 mm
Measurable Q range	$\sim$0.004–1.0 Å^{-1}
Detectable structure	0.5–150 nm
Detector available (size and resolution)	IP: 20 cm $\times$ 40 cm, 50 μm LD: 50 mm, 80 μm LD: 200 mm, 200 μm
Sample environment	Temperature: −30 °C to 300 °C Pressure: 50 mTorr–1 ATM Gas: He, N_2, Ar, O_2
Sample type	Films, solutions and solid samples

Sitting in front of the exit Kapton window of the vacuum pipe, is a beam stopper made of 1 mm thick Ta disk. The beam stopper size can be chosen from disks of 4, 6, 7 or 8 mm diameter. The beam stopper is positioned by the alignment laser and a removable photodiode. Right behind the beam stopper position and before the exit of the vacuum pipe, there is space for an imaging plate of 400 mm by 200 mm area. After exposure, 2D scattering patterns collected by imaging plates can be read out with a position resolution of 50 μm by a BAS 2500 Fuji IP reader within a few minutes.

Attached to the exit of the post-sample pipe is a 50 mm linear detector, with 80 μm position resolution. The detector uses a constant flowing P10 gas (90% argon and 10% methane) under a pressure of 7.5 bars. In front of the linear detector, there is an adjustable slit controlling the intensity and Q resolution for each specific data collection requirement. We summarize the characteristics of the SAXS instrument in Table 1.

3. Instrument performance

3.1. Standard samples

There are two common standard samples in calibrating a SAXS instrument, Ag-behenate for the calibration of instrument Q value and polyethylene (PE) for the calibration of the differential cross-section per unit volume of sample, defined as the absolute intensity $d\Sigma/d\Omega = I(Q)$. Fig. 3(a) and (b) show the SAXS data for the two samples measured at our SAXS station with a beam size of 0.5 mm diameter and a beam stopper of 4 mm. With 8 keV photons and a sample-to-detector distance of 2670 mm, the minimum Q value achievable is 0.004 Å^{-1}. On the other hand, scattering in the Q range up to 1 Å^{-1} can be measured for Ag-behenate, with 22 keV photons and a sample-to-detector distance of 1100 mm. The dynamical Q range illustrated by these two measurements ($Q_{max}/Q_{min} = 250$) indicates that the SAXS instrument is suitable for probing structures of characteristic lengths ranging from 0.5 nm to 150 nm. We use the stable scattering peak of the commercial PE, $I(Q) = 36.6$ cm^{-1} at $Q = 0.023$ Å^{-1}, to

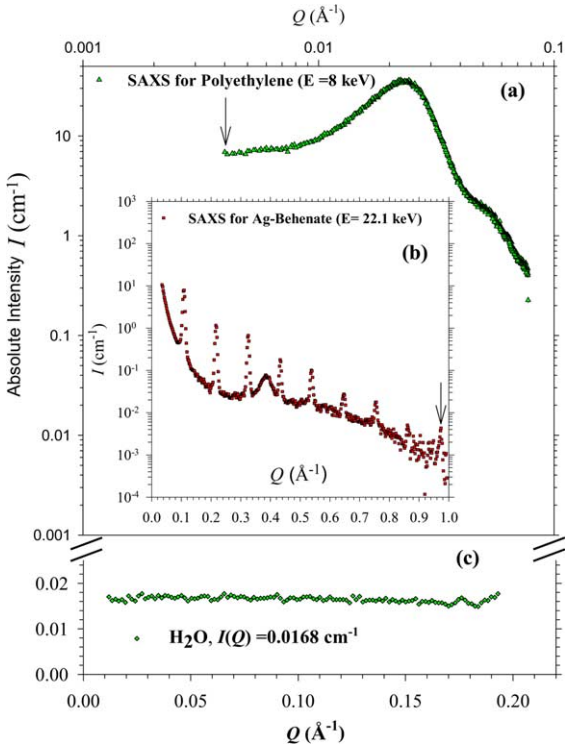

Fig. 3. SAXS data for the standard samples, polyethylene (PE) in (a) and Ag-behenate in (b), collected with photon energies of 8 keV and 22 keV, respectively. Also shown in (c) are the data collected for water, with $I(Q)$ mutual-calibrated with PE.

obtain the scaling constant between the measured $I(Q)$ and the calibrated $I(Q)$ [6]. The scaling constant then can be applied to other samples for the absolute intensity scale. With the scaling constant determined by PE, we obtained an averaged $I(Q) = 0.0168 \pm 0.0004\ \mathrm{cm}^{-1}$ (Fig. 3 (c)) for water measured at room temperature, which is consistent with a reported value of $I(Q) = 0.0163\ \mathrm{cm}^{-1}$ [7]. The flatness of the water scattering profile also serves as an examination of the uniformity of detector pixel sensitivity. On the other hand, the scattering peaks of Ag-behenate at $0.1078\ \mathrm{Å}^{-1}$ and the multiples, due to a characteristic spacing of 58.28 Å of the sample, are used for calibrating instrument Q values whenever instrument configuration is changed.

In the following, we illustrate more features of the SAXS instrument with measurements on block-polymer composites, Al alloys, nanoparticles and biomolecules in solutions.

3.2. Temperature-dependent SAXS: PS–PEO/CdS copolymer complex

Fig. 4 shows the SAXS data for a series of self-assembled nanocomposites of diblock copolymer PS-*b*-PEO embedded with 0.35% cadmium sulfide quantum dots (CdS QDs). Inside the composites, PEO blocks and CdS nanoparticles bind into spherical domains in the PS matrix and form an ordered structure, as evidenced by the scattering peaks observed (Fig. 4(a)). These scattering peaks, located at $Q = 0.0114$, 0.0158, 0.0203, 0.0228, 0.0281 and $0.0399\ \mathrm{Å}^{-1}$, form a Q-ratio of $1{:}2^{1/2}{:}3^{1/2}{:}4^{1/2}{:}6^{1/2}{:}12^{1/2}$. This ratio implies that the scattering is caused by either body-centered-cubic packed spheres (bcc) or simple-cubic spheres (sc). The PEO/CdS domains spacing calculated from the first peak position and the sc structure characteristics is 67.5 nm [8,9]. In the same figure, SAXS data for the composites added with various amounts of homopolymers of PS (hPS) and/or PEO (hPEO) (Fig. 4(a)) also exhibit similar scattering peaks as that for the composite of no blend, but with peak positions shifted to lower Q values corresponding to larger ordered spacings. The SAXS result indicates that the domain spacing of PEO/CdS in the composite can be successfully

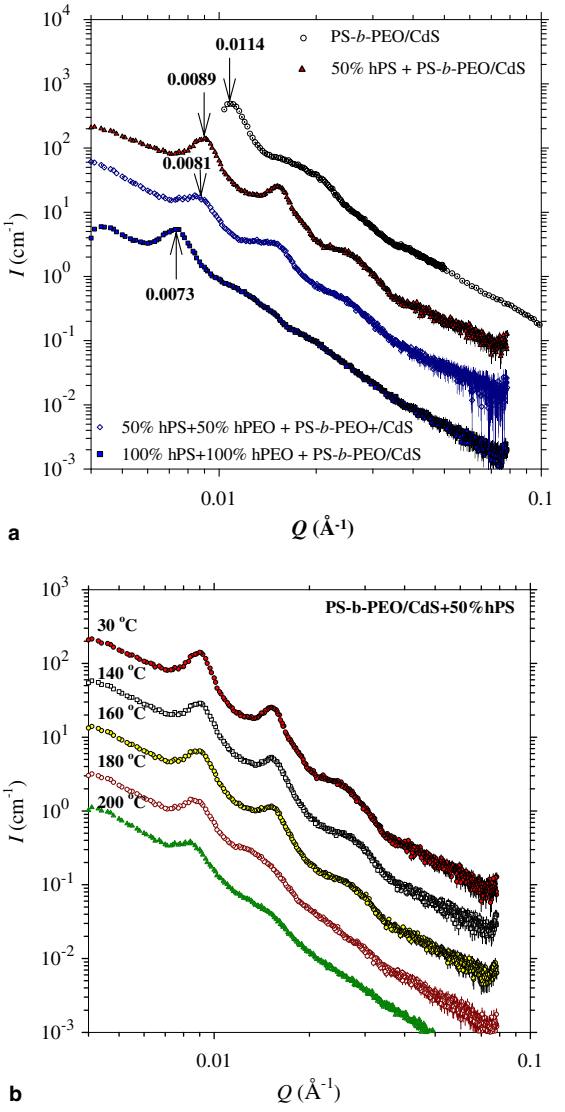

Fig. 4. SAXS data for the copolymer/nanoparticle composite PS-*b*-PEO/CdS and the composites added with various amounts of homopolymers of PS and/or PEO (hPS, hPEO). The arrows indicate the first peak positions (a). Temperature-dependent SAXS data for the composite blended with 50% hPS (b). Note, profiles in (a) and (b) are rescaled in intensity for clarity.

expanded by adding homopolymers of 50% hPS, 50% hPS + 50% hPEO or 100% hPS + 100% hPEO, to 87.0 nm, 94.7 nm or 106.1 nm, as scaled from the first peak positions. The well-resolved peaks in the small Q region manifest the good

instrumental Q resolution. Furthermore, temperature-dependent SAXS (Fig. 4(b)) shows that the composite blended with 50% hPS undergoes an order–disorder transition around 180 °C, where the scattering peaks start to broaden and the ordered structure deteriorates.

3.3. Asymmetrical SAXS patterns: crystallization kinetics of a diblock copolymer

The SAXS study demonstrated here is for the slow dynamics of P4VP-*b*-PCL block copolymers, poly(4-vinylpyridine)-block-poly(ε-caprolactone), of shear-oriented lamellar microdomains. The 2D SAXS pattern was first taken with an imaging plate at a sample temperature of 80 °C (Fig. 5(a)). At this temperature, the crystalline structure of PCL melts and leads to an enhancement of the scattering contrast between the P4VP and PCL blocks. The preferred orientation of the lamellar structure of the system is revealed by the preferred scattering direction captured in the 2D image (the dashed arrow in Fig. 5(a)). With the sample temperature dropped down quickly from 80 °C to 30 °C within a few minutes, we took time-dependent SAXS images during the crystallization of the PCL blocks under the hard 2D confinement of P4VP [10]. The series SAXS patterns taken after sample temperature dropped down to 30 °C (Fig. 5(b)–(d)) exhibit a trend of loosing the lamellar peaks due to the time-dependent crystallization of the PCL blocks, whose electron density gradually grows close to that for P4VP blocks, thus, reducing the X-ray scattering contrast and blurring the lamellar characteristic scattering peaks.

3.4. High energy SAXS: Structural evolution of Ai–Mg–Si alloys

Recently, it was reported that there was no real success for X-ray scattering in observing nano-scaled precipitates of Mg–Si formed in a matrix

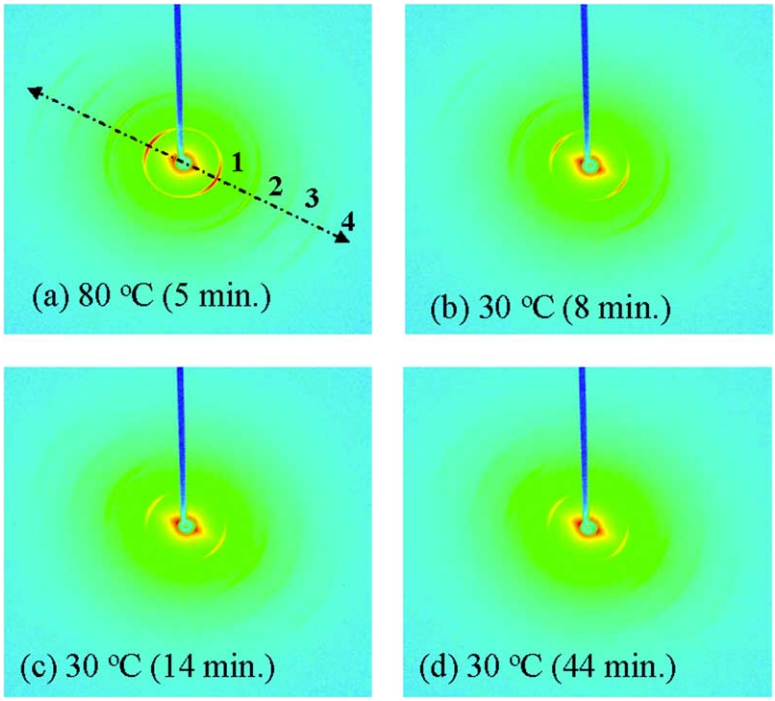

Fig. 5. Temperature-jump for time-dependent SAXS on a P4VP-*b*-PCL copolymer system. The 2D scattering patterns are collected at a sample temperature of 80 °C (a), and subsequently at 30 °C, (b)–(d), during the crystallization of the PCL blocks. The arrow in (a) indicates the normal direction of the oriented lamellar microdomains in the system.

of Al, a neighboring element of the precipitates [11]. In practical experimental considerations, the very low contrast between the precipitates and the matrix, the dilute precipitates and the high photon attenuation of Al–Mg–Si alloys restrict SAXS from the structural study of this type of materials. For instance, the sample thickness for the optimum e^{-1} transmission is 100 μm for Al–Mg–Si alloys, when 8 keV photons are used for SAXS. This requires lots of efforts in grinding samples down to thin foils. In return, the thinner sample gives a smaller scattering volume. Here, using 15 keV photons for an Al–Mg–Si alloy of 0.5 mm thick, resulting in a sample transmission of 0.33, we demonstrate that not only the morphology but also the growth kinetics of the Mg–Si precipitates can be studied by SAXS.

Fig. 6 shows the SAXS data collected between 30 °C and 260 °C for a commercial Al–Mg–Si alloy containing 1–2% of Mg and Si. During the initial stage of the heat treatment, we observed an increase in the scattering intensity only when the temperature reached 180 °C, a commonly used aging temperature in industry. From 180 °C to 260 °C, the increase in intensity under a similar scattering profile in the Q range of ~0.03–0.1 Å^{-1} indicates a multiplication of similar small precipitates in the alloy during the initial stage of the temperature-controlled aging. Whereas, in the middle (4 h at 260 °C) and late stages (more than 4 h at 260 °C), we observed significant changes in the scattering profiles, implying changes in the morphology of the precipitates during these two stages. Observation of Mg–Si precipitates in Al–Mg–Si alloys is usually limited to the TEM technique. Here, we demonstrate that our SAXS is sensitive to the morphology change of the precipitates. Furthermore, the time-dependent SAXS data collected can also reveal the growth kinetics of the precipitates, which will be very difficult to be captured by the TEM technique, especially the growth information in the initial stage. We describe the Mg–Si precipitates observed in the initial stage with a rod-like shape of a rod length of ~120 Å and a radius of ~30 Å (dashed curve in Fig. 6), basing on the Kratky–Porod approximation of the SAXS data [12] and the TEM result. It is believed that precipitates of this or similar size take a decisive role in reinforcing the mechanical strength of the alloys. The deviation in the low-Q region between the data and fitting curve is attributed to the Q^{-4} scattering contribution from precipitation-independent large particles neglected in the fitting.

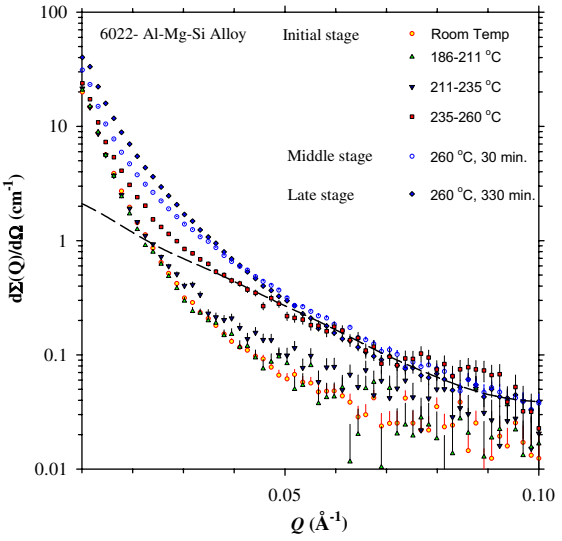

Fig. 6. Time-dependent SAXS data collected during the initial stage (30 to 260 °C), the middle stage (within 4 h at 260 °C) and the late stage (larger than 4 h at 260 °C) of an Al–Mg–Si alloy during aging. The dashed curve for a rod-like form factor of a rod length of 300 Å and a rod radius of 29 Å simulates the Mg–Si precipitates formed in the middle stage.

3.5. Anomalous SAXS: PtRu nanoparticles embedded in carbon matrix

To illustrate the advantage of the wide energy spectrum available at our SAXS station, we present an anomalous SAXS (ASAXS) study on a PtRu/C system where Pt/Ru nanoparticles are buried inside fine carbon grains. With photons energy tuned near to the K-absorption edge of Ru, we have observed that the ASAXS intensity for the PtRu/C powder drops from the off-resonant scattering curves measured with 10.353 and 11.548 keV photons (Fig. 7) in the lower-Q region. Since the scattering length of the resonant atoms is ~10% smaller than that at the off-resonant condition, we can identify the structural characteristics of the resonant atoms from the differences in the

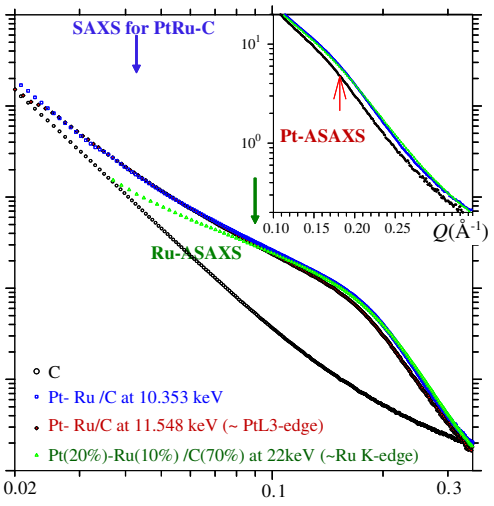

Fig. 7. ASAXS for PtRu nanoparticles performed at the 22.11 keV near the K-absorption of Ru, 11.548 keV near the L_{III}-absorption edge of Pt and an off-resonant energy 10.354 keV. SAXS data collected for the carbon matrix without PtRu nanoparticles are also shown. Inset expands the data in the higher-Q region for a clearer ASAXS effect.

SAXS and ASAXS profiles due to the change of the scattering contrast [13]. The drop of the ASAXS intensity in the lower Q region due to the Ru resonant scattering indicates a reduction of scattering contrast in the larger length scale of the system. This implies that Ru dominates the outer (or larger) structure of the PtRu nanoparticles. In contrast, with the photon energy tuned close to the L_{III}-absorption edge of Pt, the ASAXS intensity in the higher-Q region (see the inset) drops from that measured at 10.353 and 22.117 keV, indicating that Pt dominates the smaller structure of the PtRu nanoparticles. All these complimentary evidences obtained from the two ASAXS and one SAXS profiles leads us to a conclusion that PtRu nanoparticles have a core(Pt)–shell(Ru)-like structure.

3.6. Folding and unfolding of lysozyme

SAXS application on protein morphology in solution is often hindered by unwanted aggregations or damages of the proteins due to radiation absorption [14]. In circumventing the radiation effects in protein solution scattering, high energy photons may be advantageous owing to the less photo-electric absorption of protein molecules to high energy photons. In our SAXS station, we have successfully avoided the radiation-induced protein aggregation using 15 keV photons and observed the folding and unfolding morphologies of lysozyme in aqueous solutions. For details, 7 mm thick aqueous solution, of a lysozyme concentration of 21 mg/ml with 0.1 M NaCl, 0.1 M sodium citrate and 8 M urea, was sealed by two thin quartz widows of 20 μm thick each, resulting in a transmission of 0.34 (for sample with windows). During the 30 min, typical data taking with a linear detector, we kept the sample solution constantly moving within 2 mm by 2 mm area to dissipate the radiation heat from the illumination of X-rays. With all these efforts together, we could observe the low scattering intensity from lysozyme with clean background. Fig. 8 shows the scattering patterns of the reversible folded and unfolded lysozyme between 30 °C and 60 °C. The SAXS data collected at different temperatures are described (dashed curves in Fig. 8) by an ellipsoidal particle model with semi-major axis a and semi-minor axis

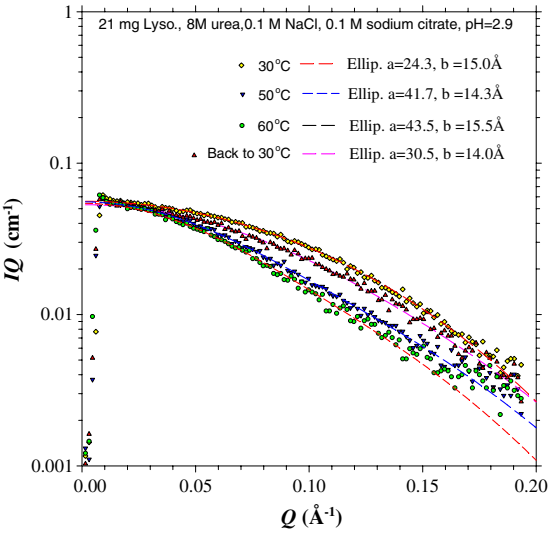

Fig. 8. Temperature-dependent SAXS data for the folding, unfolding and refolding of lysozyme in an aqueous solution of a concentration of 21 mg/ml, with 8 M urea, 0.1 M NaCl and 0.1 M sodium citrate for pH 2.9. The data are simulated (dashed curves) using a form factor of ellipsoidal shape with semi-major axis a and semi-minor axis b.

b. The radii of gyration R_g, 14.4 ± 0.5 Å and 22.5 ± 0.5 Å, calculated from the ellipsoidal sizes fitted for the folded and unfolded lysozyme agree with the literature values obtained from the Guinier approximation [15]. Here, we would like to emphasize that the volume ratio of the unfolded and folded lysozyme, an interested quantity in some theoretical model for folding free energy [16], cannot be scaled simply from R_g^3 values, since this will result in an unrealistic expectation for a large volume expansion in protein unfolding, especially when the protein shape deviating significantly from a globular shape, as the case we observed for the unfolded lysozyme.

4. Concluding remarks

We have constructed a SAXS instrument and conducted several measurements to demonstrate the performance of the instrument, including the ASAXS for the PtRu/C system, the Al–Mg–Si alloy and the solution SAXS for lysozyme, which are difficult to have quantitative results with in-house X-ray sources. We emphasize the advantages of using higher X-ray energy SAXS in certain research topics.

Acknowledgements

A dedicated instrument is always supported by many people who contribute here and there. For this, we thank C.H. Chang, S.H. Chang, C.Y. Liu, D.G. Liu, J.F. Lee, H.S. Sheu, Z.M. Huang, C.H. Hsu, M.T. Tang, Y.S. Huang and J.M. Juang. We thank Drs. C.S Tsao, J.S. Lin, S.W. Yeh and R.M. Ho for providing samples.

References

[1] T. Fujisawa, K. Inoue, T. Oka, H. Iwamoto, T. Uruga, T. Kumasaka, Y. Inoko, N. Yagi, M. Yamamoto, T. Ueki, J. Appl. Crystallogr. 33 (2000) 797.
[2] B. Chu, B. Hsiao, Chem. Rev. 101 (2001) 1727.
[3] T. Narayanana, O. Diatb, P.B. Oseckea, Nucl. Instr. and Meth. A 467–468 (2001) 1005.
[4] H. Amenitsch, S. Bernstorff, P. Laggner, Rev. Sci. Instr. 66 (2) (1995) 1624.
[5] Y.F. Song, C.H. Chang, C.Y. Liu, L.J. Huang, S.H. Chang, J.M. Chuang, S.C. Chung, P.C. Tseng, J.F. Lee, K.L. Tsang, K.S. Liang, Proceedings of the 8th International Conference on Synchrotron Radiation Instruments, American Institute of Physics 0-7354-0180-2/04, 2004.
[6] T.P. Russell, J.S. LIN, S. Spooner, G.D. Wignall, J. Appl. Crystallogr. 21 (1988) 629.
[7] D. Orthaber, A. Bergmann, O. Glatter, J. Appl. Crystallogr. 33 (2000) 218.
[8] S.-W. Yeh, K.-H. Wei, Y.-S. Sun, U. Jeng, K.S. Liang, Macromolecules 36 (2003) 7903.
[9] U. Jeng, Y.-S. Sun, H.-Y. Lee, C.-H. Hsu, K.S. Liang, S.-W. Yeh, K.-H. Wei, Macromolecules 37 (2004) 4617.
[10] L. Zhu, B.R. Mimnaugh, Q. Ge, R.P. Quirk, S.Z.D. Cheng, E.L. Thomas, B. Lotz, B.S. Hsiao, F. Yeh, L. Liu, Polymer 42 (2001) 9121.
[11] H.P. Karnthaler, B. Mingler, C. Rentenberger, T. Waitz, Microsc. Microanal. 9 (Suppl. 3) (2003) 336.
[12] O. Glatter, O. Kratky, Small Angle X-ray Scattering, Academic Press Inc., London, New York, 1980.
[13] H.-G. Haubold, X.H. Wang, G. Goerigk, W. Schilling, J. Appl. Crystallogr. 30 (1997) 653.
[14] S. Arai, M. Hirai, Biophys. J. 76 (1999) 2192.
[15] L. Chen, K.O. Hodgson, S. Doniach, J. Mol. Biol. 261 (1996) 658.
[16] K.K. Liang, M. Hayashi, Y. Shiu, Y. Mo, J. Shao, Y. Yan, S.H. Lin, Phys. Chem. Chem. Phys. 5 (2003) 5300.